Microstructure and defect analysis in the vicinity of blisters in polycrystalline tungsten

A. Manhard [a,*], U. von Toussaint [a], M. Balden [a], S. Elgeti [a], T. Schwarz-Selinger [a], L. Gao [a], S. Kapser [a,b], T. Płociński [c], J. Grzonka [c,d], M. Gloc [c], Ł. Ciupiński [c]

[a] Max Planck Institute for Plasma Physics, Boltzmannstr. 2, 85748 Garching, Germany
[b] Physik-Department, Technische Universität München, James-Franck-Str. 1, 85748 Garching, Germany
[c] Warsaw University of Technology, Faculty of Materials Science and Engineering, Materials Design Division, Wołoska 141, 02-524 Warsaw, Poland
[d] Institute of Electronic Materials Technology, Wolczynska 133, 01-919 Warsaw, Poland

ARTICLE INFO

ABSTRACT

Up to now, analyzing the production of dislocation-type defects in the subsurface region of plasma or ion-exposed tungsten samples has been hampered by the challenging production of suitable cross-section samples for transmission electron microscopy. We present two reliable methods based on precision electropolishing to prepare cross-sections of tungsten that allow direct imaging of dislocation-type defects by scanning as well as by transmission electron microscopy. Using these methods, we are able to demonstrate a clear enhancement of the dislocation density in the caps of blisters on tungsten exposed to H isotope plasma, i.e., of surface morphologies that are correlated to subsurface cavities. As a benchmark, we also show a cross-section of tungsten irradiated by 20 MeV W^{6+} ions.

1. Introduction

The interaction of hydrogen isotope plasmas with tungsten (W) has been investigated in many laboratory experiments. In such experiments, surface features with correlated (see [1] and references therein) and often gas-filled [2] subsurface cavities are commonly observed. Such features are also occasionally observed in fusion experiments, particularly on polished surfaces (see, e.g., [3]). Although many different classes of these features exist, they are usually all named "blisters", regardless of their shape and formation mechanism. Which types of them occur depends on many experiment parameters, e.g., material grade, sample temperature, ion energy, ion flux and ion fluence (see, e.g., [1] and references therein). A common property of blisters is that if they occur, the hydrogen isotope retention after plasma exposure is often particularly high, too. Unfortunately, it is still to a large extent unclear how blister nucleation works in detail, specifically also for W. Basically, it is thought that plasma exposure of tungsten causes a supersaturation with H isotopes in solid solution. These then precipitate as molecules, for example at pre-existing defects. The increasing gas pressure then leads to the growth of blisters [2]. Examples of proposed blister formation mechanisms for various metals and hydrogen loading conditions are given, e.g., by Condon and Schober [4]. Similarly, it is not yet clear by which mechanisms blistering influences H isotope retention. Gas filling of blisters has been experimentally validated for some cases [2], but the blister-related formation of other traps for H isotopes, e.g., dislocation-type lattice defects, has only been shown indirectly (see, e.g., [5,6]). One hypothesis is that the material surrounding a growing blister cavity is subjected to plastic deformation, i.e., dislocations are produced and moving. These would serve as additional traps for H isotopes, thus enhancing H isotope retention [5].

The standard imaging method to investigate dislocation-type defects is transmission electron microscopy (TEM). Typically, very thin samples with a thickness of the order of 100 nm are required for this. To achieve such small thicknesses, the last thinning step is, for example, performed by sputtering with an ion beam. Recently, also the preparation of pinpoint cross-section lamellae by focused ion beam (FIB) milling has become popular for a range of materials. Unfortunately, a high density of nanoscale defects is introduced into the sample by ion beams, which is reported to be partially removable by low-energy argon ion milling (see, e.g., [7,8]). For tungsten, usually only electrochemical thinning (see, e.g., [9]) is able to produce samples entirely without such preparation artifacts. However, electropolishing works reliably only for conventional TEM samples made from bulk material. The well-proven

* Corresponding author.
  E-mail address: armin.manhard@ipp.mpg.de (A. Manhard).

electrolytes for bulk polishing or TEM samples have high material removal rates, so the required polishing time for a ~100 nm thin sample is extremely short. Electrochemical treatment of already thinned samples is therefore often referred to as "flash polishing". Unfortunately, flash polishing recipes are not well documented. Its application to the fragile lamellae produced by FIB is associated with a high failure rate. In conjunction with the preparation effort for the FIB lamella in the first place, the work effort to produce a sample by flash polishing is usually considered prohibitive.

In this article, we present two novel methods for the preparation of cross-section slices of plasma-exposed tungsten. These cross-sections allow the direct imaging of dislocation-type defects, one by scanning electron microscopy (SEM) and one by TEM. Up to now, it was extremely challenging to produce cross-section slices of sufficient quality to clearly identify these defects. With our methods we have found an efficient way for producing high-quality cross-section samples that allow dislocation imaging. In addition to describing these sample preparation techniques, we present first direct evidence of a clear enhancement of the dislocation density in blister caps.

2. Cross-section preparation

2.1. Bulk cross-sections

To avoid the difficulties mentioned above and to find more reliable ways of preparing cross-sections for dislocation imaging, we have approached the problem from two sides. One is to avoid the fragile FIB lamellae altogether and instead to electropolish bulk cross sections. On these, electron channeling contrast imaging (ECCI) using a high-resolution SEM can also reveal the dislocation structure (see, e.g., [10,11]). For this process, the sample was first cut into two or more pieces along the desired cross-sectioning direction using a diamond wire saw or a diamond cutting wheel. Two pieces of sample were then glued together with the plasma-exposed sides facing each other. During the subsequent grinding and polishing with SiC abrasive paper up to P4000 and with 3 μm diamond suspension, this protects the surfaces of interest against rounding and exfoliation. After cleaning, the sample is finally electropolished for 10–15 min in an electrolyte solution containing 300 g H_2O, 9 g NaOH and 450 g glycerol, which is slowly stirred during the polishing process. As a current-voltage curve of a larger test sample had yielded a broad plateau between 6 and 8 V in the same electrolyte without stirring, the polishing voltage was chosen to be 7 V. The addition of glycerol (which was occasionally reported before, see, e.g., [12]) increases the viscosity of the electrolyte and reduces the material removal speed to about 1 μm/min for the conditions used here. Generally, this mixture was found to yield a more even cross-section surface than using only aqueous NaOH solution. The glue layer between the two samples is not removed by the electropolishing process. Since the electrolyte is flowing across the cross-section surface due to the stirring, it is necessary to slowly rotate the sample. This serves to avoid uneven material removal on the upstream and downstream sides of the glue wall. It is important to quickly rinse the sample with de-ionized water after electropolishing has stopped in order to avoid anisotropic etching of W on the nanometer scale. Once a satisfactorily electropolished cross-section surface is obtained, the glue is dissolved in acetone, and the sample is carefully and repeatedly rinsed in de-ionized water and ultra-clean acetone to remove all glue stains. On the obtained bulk cross-sections, it is now possible to either view the top and the cross-section surface simultaneously when tilting the sample, or to perform ECCI on the cross-section surface. These bulk cross-sections are also ideally suited for analytic SEM techniques such as orientation mapping by electron backscatter diffraction (EBSD).
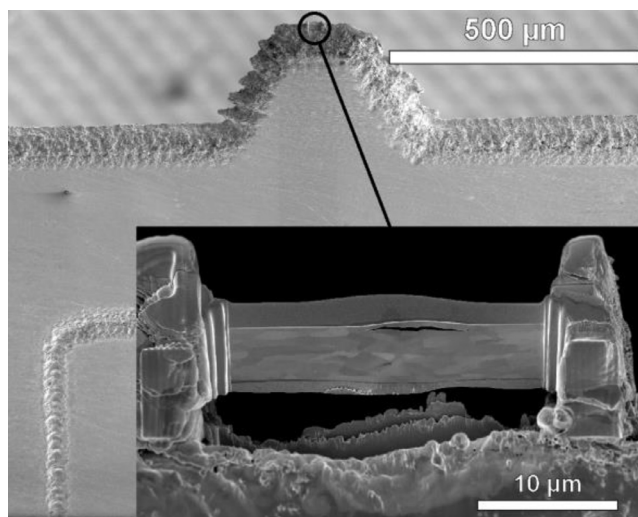

Fig. 1. W support for FIB-cut TEM lamellae. The freshly cut lamella sits on top of the small tip approximately in the center of the support (inset). Only the small tip carrying the lamella is immersed into the electrolyte for electropolishing. (*Note:* The lamella surface is tilted by 52° with respect to the viewing direction).

2.2. Cross-section lamellae for TEM

The second method was developed by further adapting the electropolishing recipe mentioned above for W to achieve very slow (~10–20 nm/min) and homogeneous material removal, together with systematically identifying and eliminating other failure risks. The desired slow material removal rate was achieved by replacing even more water by glycerol. The mixture that yielded the best results contained 150 g H_2O, 9 g NaOH and 600 g glycerol. This electrolyte is not stirred during electropolishing. The polishing voltage is 7 V. Instead of a single counter electrode, we used a pair of symmetric, parallel W plates. The support carrying the lamella (see Fig. 1) was oriented such that the lamella is parallel to the counter electrodes. Compared to a single electrode, this geometry vastly improved the homogeneity of the electropolishing process and minimized preferential etching at the thin edge of the lamella. To further protect the plasma-exposed surface of the sample, it was coated with 100 nm Pt by electron beam evaporation prior to FIB lamella preparation. This coating is resistant against the electropolishing process for W. For the FIB milling (here: FEI HELIOS NanoLab 600), an additional Pt-C protective layer of about 1.5 μm thickness was deposited in situ in the microscope to prevent surface erosion by the Ga^+ ion beam (using first Pt-C deposition by e^- beam for marking the region of interest and then the Ga^+ ion beam for depositing the actual protection layer). However, this coating shows only limited resistance against electropolishing: The C is leached from the layer and leaves a sponge-like Pt structure, and in some cases the layer detaches from the W. The Pt film deposited by electron beam evaporation showed no such behavior.

To avoid parasitic electrochemical reactions, W supports (see Fig. 1) were used for mounting the FIB-cut lamellae instead of the standard Cu supports. Indeed, tests showed that Cu is attacked during the electropolishing process. Only the tip of the support where the lamella was attached was immersed in the electrolyte. The support itself was held by reverse-action tweezers. Care was taken to avoid contact between the electrolyte and the tip of the tweezers.

Another important part for improving the reliability of the process was to enhance the attachment of the lamella to the W support. After a preliminary gluing by Pt-C deposition from the top of the lamella, the sample was tilted and four more gluing
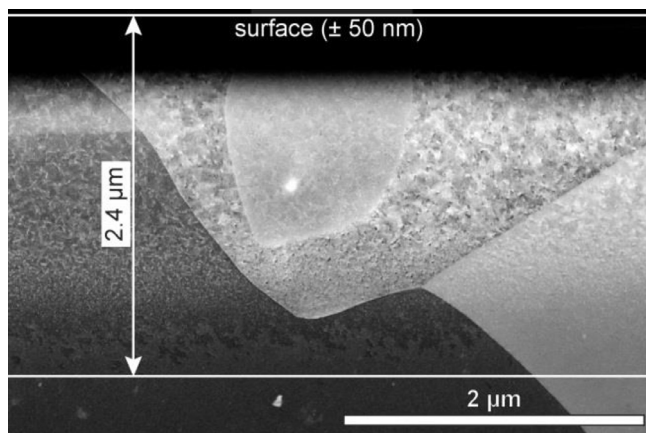
Fig. 2. ECCI cross-section image of recrystallized W damaged by 20 MeV W^{6+} ions. A high density of dislocations is visible below the sample surface and tails out into many small dislocation loops towards the ultimate depth of the ion-affected zone of ~2.4 μm.

Fig. 3. ECCI cross-section image of a blister cavity in recrystallized W exposed to high D ion flux (~10^{22} D/m^2s) and fluence (10^{27} D/m^2) at an ion energy of 38 eV/D and a temperature of 515 K. The sample has been heated to 1200 K for TDS. This kind of blister morphology is most likely be produced by plastic deformation of W induced by dislocation sliding at low-indexed slip systems during plasma exposure [13]. While the dislocation density is very low throughout most of the sample, a high concentration of dislocations is visible in a region above the blister cavity.

strips of Pt-C were placed across the interface between support and lamella, one at each corner of the lamella. This was because we found that one of the main causes of failure for our process was that the lamella broke off either during immersion in the electrolyte or during the subsequent washing in de-ionized water and ultra-clean acetone.

Observing these points, the rate of failure was reduced significantly. The complete loss of a lamella was practically totally excluded, and with an initially 200 nm thick lamella, 3 minutes of electropolishing were possible until a small hole appeared in a region where the sample had slightly buckled during the final FIB thinning, and thus was thinner than 200 nm. As long as the lamella is still thick enough, the electropolishing process can be repeated several times. As a test, one initially 100 nm thick lamella was polished subsequently for 60 seconds, 30 seconds and again 30 seconds. Therefore, we would call our method precision electropolishing rather than flash polishing.

Unfortunately, it appears that removing approximately 50 nm from each side during 3 minutes of electropolishing (i.e., starting from a 200 nm thick lamella and targeting a 100 nm thick lamella) is not sufficient to completely remove the damage introduced by FIB. (For all FIB process steps, an acceleration voltage of 30 kV was used, and the sample was tilted by 2° relative to the ion beam to compensate for beam divergence). Although the sample quality improves substantially, still a significant number of the dot-like defects typically found after ion FIB milling remain, which on high magnification appear to be small dislocation loops. We therefore conclude that the initial lamella thickness should be closer to 300 nm, which would also make the FIB thinning process faster and less risky in terms of, e.g., lamella buckling.

3. Results

3.1. Bulk cross-section

As a benchmark for the image quality of bulk cross-sections, we first investigated a polycrystalline W sample that was electropolished, recrystallized for 2 min at 2000 K and subsequently damaged by implanting 20 MeV W^{6+} ions with a fluence of 7×10^{17} W ions/m^2 (see Fig. 2). Using the preparation method described in Section 2.1, we were able to qualitatively reproduce earlier observations by Ciupiński et al. [7] and Grzonka et al. [8]. In direct comparison, the depth of about 2.4 μm that is affected by the MeV ion implantation is closely reproduced. The ultimate range of the damage caused by the MeV ions is well visible in
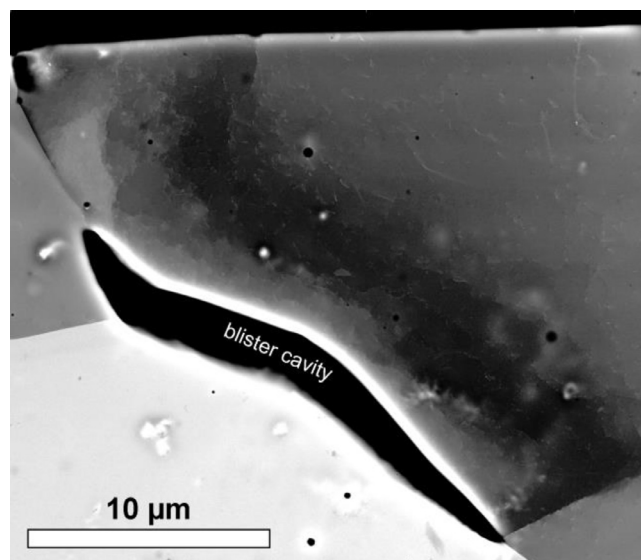
the bulk cross-section due to the complete absence of FIB-induced defects. The drawbacks are that the information volume for ECCI with 30 keV electron energy is smaller than for TEM with 200 keV. It is of the order of the elastic mean free path, i.e., roughly 20 nm in W [13]. In addition, TEM yields images with slightly better contrast and less noise, and a narrow region adjacent to the sample surface is often blacked out in a high-contrast ECCI image (but can be clearly seen in a secondary electron image). A major advantage of our bulk cross-sectioning technique is that it allows investigating cross-sections with very large dimensions both in the lateral and in the thickness direction, i.e., across an entire sample. This makes it possible to perform investigations with high statistical relevance.

We then applied the bulk cross-sectioning technique to a recrystallized W sample exposed to a high-flux (~10^{22} D/m^2s), high-fluence (10^{27} D/m^2) deuterium (D) plasma. The ion energy was 38 eV/D, and the sample temperature was 515 K. Thermal desorption spectroscopy (TDS) was also performed on this sample, which entails heating up to ~1200 K. The sample exhibits mainly large "table-top mountain" surface structures, which originate from a cavity at a grain boundary. This sample was part of a series of samples that were investigated by Alimov et al. [14] and Lindig et al. [15]. From FIB cross-sectioning and orientation mapping of the grains containing this kind of blisters, it was concluded that these surface features are formed by plastic deformation of W induced by dislocation sliding at low-indexed slip systems from the cavity to the surface. Using the bulk cross-sectioning method described here, we are now able to directly observe the impact of such features on the dislocation density in the surrounding W material. The ECCI cross-section image of a blister in Fig. 3 was acquired with a FEI HELIOS NanoLab 600 microscope at an acceleration voltage of 30 kV using the concentric backscatter (CBS) detector. In the case shown here, the part of the blister protruding above the surface cannot be seen because, as explained by Lindig et al. [15], it is not located directly above the cavity.

In a relatively sharply defined region above the blister cavity, lattice deformations are visible as variations in grayscale contrast.
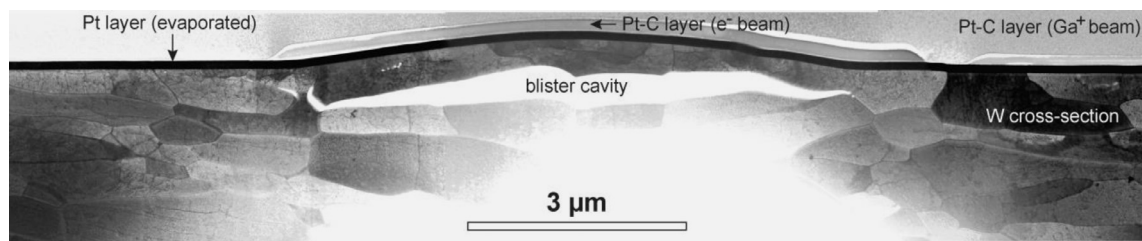
Fig. 4. Bright-field cross-section STEM image of a dome-shaped blister in hot-rolled, polycrystalline W at a grain boundary parallel to the plasma-exposed surface. The sample was exposed to D plasma at an ion flux of 10^{20} D/m^{2}s to a fluence of 6×10^{24} D/m^2 at an ion energy of 38 eV/D and a temperature of 300 K. The sample has been heated to 1200 K for TDS. The image is a composite of 5 individual micrographs. In addition to dislocations in grains throughout the material, a particularly high dislocation density is visible in the blister cap. Small, dot-like defects caused by FIB milling are still visible despite substantial thinning by electropolishing (see also Figs. 5 and 6b).
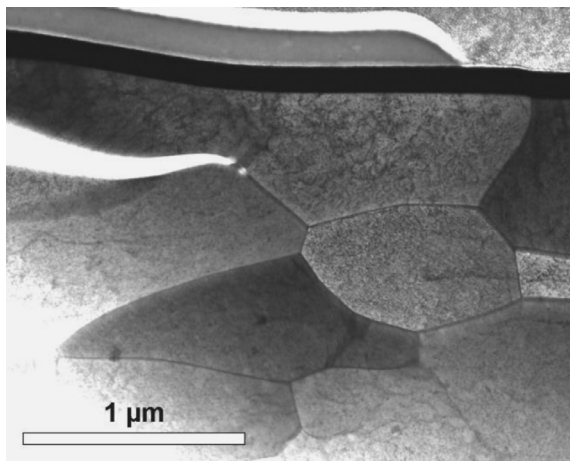

Fig. 5. Close-up STEM image (bright field) of the blister shown in Fig. 4. The image shows the surroundings of the crack-tip on the right hand side. The dislocation networks are particularly dense in the blister cap. In addition, small, dot-like defects resulting from the FIB preparation are still visible (see also Fig. 6b).

These are accompanied by a high density of dislocations, which are visible as bright lines on darker background in this contrast mode. Outside of this zone, the dislocation density is almost undetectably low. Generally, dislocations were almost exclusively found in the immediate vicinity of blisters. Small, circular cavities, which are visible in Fig. 3 as dark spots, were already present in the initial material (i.e., without any plasma exposure).

3.2. Cross-section lamella for TEM

For preparing a thin cross-section lamella for TEM by FIB milling, a hot-rolled polycrystalline W sample exposed to D plasma with an ion flux of 10^{20} D/m^{2}s to a fluence of 6×10^{24} D/m^2 was used. The ion energy was 38 eV/D, the sample temperature was 300 K. Under these conditions, many relatively small (typical diameter ≤ 10 μm), dome-shaped blisters form on the plasma-exposed surface (see, e.g., [2,15]). Their corresponding cavities are located at grain boundaries parallel to the surface in typical depths of about 1 μm. The small size and shallow depth make these blisters ideal objects of study for TEM. The sample used here also underwent TDS, after which most blisters had fully collapsed (see [16]). The blister whose cross-section is shown in Fig. 4 is one of the few remaining ones, which were inflated to the point of plastic deformation by the plasma exposure.

Fig. 4 shows a composite image constructed from 5 individual bright-field images. Fig. 5 shows a close-up of the crack tip region on the right hand side of the blister. They were acquired using a FEI HELIOS NanoLab 600 microscope at 30 kV acceleration voltage with the retractable STEM (scanning transmission electron microscopy) detector. On top of the W surface, the Pt layer produced by electron beam evaporation (dark band), and two layers of Pt-C deposited in situ in the microscope are visible. The thin smooth layer on top of the blister was deposited using the electron beam and served to mark the location for the cross-section slice. The grainier layer on top was deposited by the Ga$^+$ ion beam in order to protect the surface from erosion during FIB milling. Both layers show imperfect attachment in some locations after electropolishing. Particularly from the coarse-grained layer, also the carbon was leeched, leaving a porous, sponge-like structure. This emphasizes the necessity of the dense pure Pt layer, which remained unaffected. Unfortunately the lamella had slightly buckled during the final stages of FIB milling, so a small area directly below the blister had become very thin. In this area, a perforation of the lamella occurred during electropolishing, which is visible as the white area below the blister cavity.

Throughout this cross-section lamella, one can clearly recognize dislocation networks, as it would be expected from prior microstructure analysis of the original material [9]. Some grains show somewhat blurred dislocations, since the sample is relatively thick considering the low acceleration voltage of 30 kV used here. In other grains, the dislocations appear clear and crisp, most likely thanks to channeling increasing the mean free path of the electrons. Strong thickness variations between individual grains are unlikely, since these were not observed in secondary electron images of the lamella. Unfortunately, even the already substantial material removal by electropolishing (about half of the initial lamella thickness!) was not sufficient to completely remove the dot-like defects introduced by FIB milling (see also Figs. 5 and 6b), as already mentioned in Section 2.2.

The density of the dislocation networks in the blister cap, particularly at the apex and *above* the "hinge" regions of the cap, appears to be substantially higher than in other locations of the sample. Interestingly, no pronounced dislocation tails are visible emanating from the crack tips (see also Fig. 5).

Another interesting feature of this sample is that within the first layer of grains, a significant number of small, circular or elliptical cavities are found (see Fig. 6). Within the area depicted in Fig. 6a, 32 such cavities were identified, using 3 micrographs at different tilt angles in order to optimize cavity visibility. Their average equivalent diameter is 25 ± 14 nm. The smallest cavity found here has an equivalent diameter of only 9 nm. The largest ones are up to 72 nm large and actually appear to consist of two or more merged bubbles. In contrast to the small cavities in the bulk cross-section described in Section 3.1, these do not appear deeper within the sample. The deepest of these nano-cavities occur directly at the first grain boundary parallel to the surface, which is, in the case of Fig. 6, located about 250–400 nm below the surface. It is therefore likely that these features are indeed a consequence of the plasma exposure, although their final appearance may be influenced also by the subsequent TDS. Another interesting property of these cavities is that they seem to preferably occur in small groups, often aligned like beads on a string.
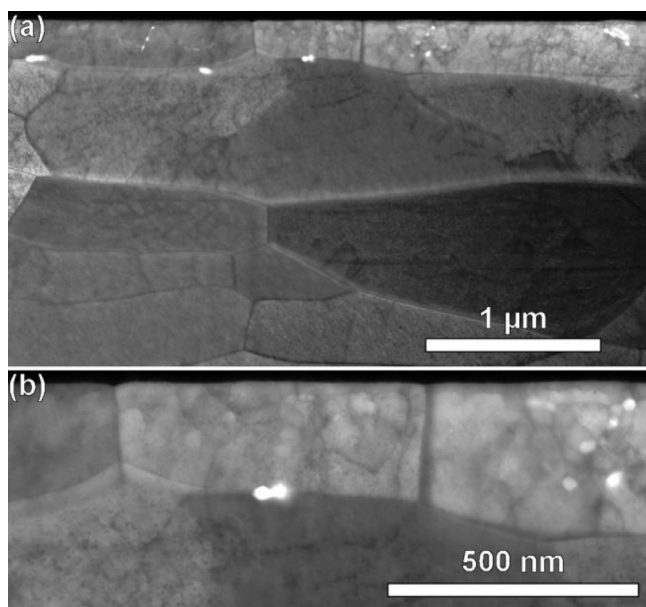
Fig. 6. Nanoscopic cavities within the first grain layer of hot-rolled, polycrystalline W exposed to D plasma. The image is from the same sample as shown in Fig. 4, but depicts an adjacent area of the cross-section lamella. 32 of these nano-pores can were identified in the region depicted in panel (a). Panel (b) shows a close-up of the central near-surface area.

4. Discussion

Both from the bulk cross-section of recrystallized W (Fig. 3) and the TEM cross-section of hot-rolled W (Fig. 4), it is evident that the formation of different kinds of blisters can indeed cause a substantial local increase of the dislocation density. For such a "table-top mountain", the dislocation-rich zone appears to be sharply delimited. Considering that the proposed formation mechanism is plastic deformation of W induced by dislocation sliding at low-indexed slip systems [15], this appears reasonable. First indications for such strongly deformed glide zones were already made by SEM observation of FIB cross-sections (e.g., [1]). The particular case investigated here is an ideal candidate for such an observation, since the background density of intrinsic dislocations is very low, and the preparation method for the cross-section fully eliminated any preparation-induced dislocation-type defects.

For the TEM cross-section of hot-rolled W, the analysis is a bit more difficult since the intrinsic dislocation density resulting from the hot-rolling process, as derived from STEM bright-field images of samples prepared from bulk W [9], is already considerable, namely $\rho_{disloc} = (3.2 \pm 1.7) \times 10^{14}$ m/m^3. Also, there are still dot-like defects due to FIB preparation present in the sample, which make the accurate identification of dislocations more challenging. To derive actual dislocation densities from the image in Fig. 4, the dislocations were first traced manually. We then calculated the local average of the dislocation density using a normalized Gaussian filter with a square kernel of 361×361 nm^2 (101×101 pixels^2) and $\sigma/\sqrt{2} = 143$ nm (40 pixels) (see Fig. 7). Of course, due to the limited statistics and the challenges of reliably identifying dislocations, this locally averaged density should only be seen as an estimate. Nevertheless, assuming a sample thickness of about 100 nm, this analysis yields a bulk dislocation density of around $1–2 \times 10^{14}$ m/m^3. Considering the aforementioned uncertainties in the data evaluation, this is in reasonable agreement with the previously determined dislocation density of the pristine material [9]. The peak dislocation densities determined here range up to above 7×10^{14} m/m^3 near the cap hinges, which is significantly higher than the bulk value. Generally, the dislocation density is significantly enhanced in and next to the blister cap. Compared to finite-elements (FEM) continuum mechanics calculations for a blister with a fixed boundary that had similar dimensions as the one investigated here [17,18], the distribution of equivalent plastic strain for the case assuming an internal gas pressure of 100 MPa and a yield stress of W of 700 MPa is in excellent agreement with the locations of particularly high dislocation density in Fig. 7. This similarity, together with the absence of pronounced dislocation emission directly at the crack tips leads us to speculate that the blister grows in a step-wise manner: Brittle fracture along grain boundaries, virtually without emission of dislocations, might alternate with a state where the crack tips are temporarily pinned (e.g., by small precipitates or grain boundary junctions). In the latter state, the blister would be inflated by D permeating through the blister cap and, just like in the FEM calculations [17,18], eventually develop a plastic instability at the crack tips. This would mean dislocation emission and the formation of a kink at the blister edge. Looking at Figs. 4 and 7, one can even find a region in the blister cap where a small kink in the blister cap coincides with a peak in dislocation density (about 1.5 μm from the right-hand edge of the blister).

We applied a similar analysis technique to the blister in recrystallized W (Fig. 3). If we assume an information depth for ECCI of roughly 20 nm (see Section 3.1.), we tentatively arrive at dislocation densities between about 1×10^{14} and 4×10^{14} m/m^3 in the slip zone by using a normalized, circular Gaussian filter with 1.25 μm (200 pixels) radius and $\sigma/\sqrt{2} = 1.00$ μm (160 pixels).

Near-surface nano-cavities similar to those observed in the first grain layer of the hot-rolled W sample (Fig. 6) might be responsible for the many small bursts of D_2 release reported during sputtering with residual gas analysis [19], respectively the small, intense, localized sources of D during nano-SIMS (SIMS: secondary ion mass spectrometry) mapping of a D-implanted W sample [20]. In addition, the nano-pores located at grain boundaries might be early nucleation stages of blisters such as shown in Fig. 4, while those appearing in string-like groups could eventually develop into intra-granular cracks with corresponding flat-topped surface protrusions. Such protrusions are discussed, e.g., by Lindig et al. [15] and Gao et al. [21], and are also found on the surface of the sample from which the cross-section shown in Fig. 4 was produced. In some cases, a fine crack connecting several nano-pores can actually be seen in Fig. 6a. As mentioned before, the circular cavities found in the recrystallized W sample were already present in the initial material. Most likely, D_2 gas also precipitates into such pre-existing cavities during plasma exposure.

5. Summary

We have demonstrated two different, novel routes in order to obtain high-quality cross-section samples from W. One is to prepare metallographic bulk cross-sections and to subsequently electropolish them with an electrolyte consisting of water, NaOH and glycerol. Electron channeling contrast imaging (ECCI) then allows direct imaging of dislocation-type defects. This method was verified by analyzing a cross-section sample of recrystallized W damaged by 20 MeV W^{6+} ions and comparing the image to literature data [7,8]. The other route is to prepare cross-section lamellae by FIB, but with a substantially larger thickness than it would be needed to obtain TEM images. These lamellae are then further thinned by precision electropolishing. For this, a variant of the electrolyte for polishing bulk cross-sections was used where the ratio of glycerol to water was increased even further. First results obtained with the help of these two techniques demonstrate that the dislocation density can be significantly increased in blister caps. In the case of a dome-shaped blister created by D
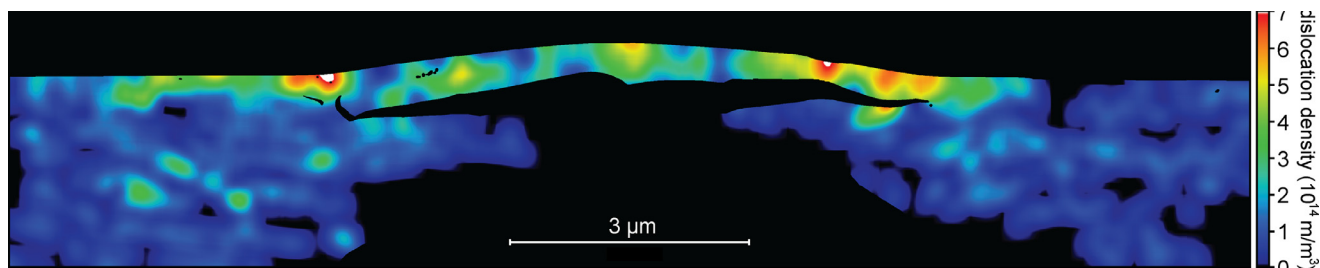
Fig. 7. Locally averaged dislocation density corresponding to the image shown in Fig. 4. The dislocation density was computed using a normalized 361×361 nm^2 (101×101 pixel^2) Gaussian kernel with $\sigma/\sqrt{2} = 40$. It is clearly enhanced in the blister cap, particularly near the "hinge" regions.

plasma exposure of hot-rolled, polycrystalline W at 300 K, peak dislocation densities of more than 7×10^{14} m/m^3 were found. This is significantly above the bulk value. We also found evidence for nanoscopic, circular or elliptical cavities. In the case of hot-rolled W exposed to a D flux of 10^{20} D/m^{2}s at 300 K, the exclusive occurrence of such cavities in close proximity to the plasma-exposed surface points strongly towards a plasma-induced origin.

Acknowledgment

References

[1] M. Balden, A. Manhard, S. Elgeti, J. Nucl. Mater. 452 (1–3) (2014) 248–256, doi:10.1016/j.jnucmat.2014.05.018.

[2] M. Balden, et al., J. Nucl. Mater. 414 (1) (2011) 69–72, doi:10.1016/j.jnucmat.2011.04.031.

[3] M. Balden, et al., J. Nucl. Mater. 438 (2013) S220–S223, doi:10.1016/j.jnucmat.2013.01.031.

[4] J.B. Condon, F. Schober, J. Nucl. Mater. 207 (1993) 1–24, doi:10.1016/0022-3115(93)90244-S.

[5] A. Manhard. (Ph.D. thesis), Deuterium Inventory in Tungsten After Plasma Exposure: A Microstructural Survey, Augsburg University, 2012, https://opus.bibliothek.uni-augsburg.de/opus4/frontdoor/index/index/docId/1981.

[6] A. Dubinko, et al., Phys. Scr. T167 (2016) 014030, doi:10.1088/0031-8949/T167/1/014030.

[7] Ł. Ciupiński, et al., Nucl. Instrum. Methods B 317A (2013) 159–164, doi:10.1016/j.nimb.2013.03.022.

[8] J. Grzonka, et al., Nucl. Instrum. Methods B 340 (2014) 27–33, doi:10.1016/j.nimb.2014.07.043.

[9] A. Manhard, M. Balden, S. Elgeti, Pract. Metallogr. 52 (8) (2015) 437–466, doi:10.3139/147.110354.

[10] I. Gutierrez-Urrutia, S. Zaefferer, D. Raabe, Scr. Mater. 61 (2009) 737–740. dx.doi.org/10.1016/j.scriptamat.2009.06.018.

[11] I. Gutierrez-Urrutia, S. Zaefferer, D. Raabe, J. Min. Met. Mater. Soc. 65 (9) (2013) 1229–1263, doi:10.1007/s11837-013-0678-0.

[12] R. Bernstein, J. Bremer, Surf. Coat. Technol. 31 (3) (1987) 297–302, doi:10.1016/0257-8972(87)90082-X.

[13] A. Jablonski, F. Salvat, C.J. Powell, NIST Elastic Electron Scattering Cross-Section Database (SRD 64), National Institute of Standards and Technology, Gaithersburg, MD (USA), 2010 version 3.2 http://www.nist.gov/srd/nist64.cfm.

[14] V. Kh. Alimov, et al., Phys. Scr. T138 (2009) 014048, doi:10.1088/0031-8949/2009/T138/014048.

[15] S. Lindig, et al., Phys. Scr. T138 (2009) 014040, doi:10.1088/0031-8949/2009/T138/014040.

[16] A. Manhard, et al., J. Nucl. Mater. 415 (2011) S632–S635. dx.doi.org/10.1016/j.jnucmat.2010.10.045.

[17] J.-H. You, J. Nucl. Mater. 437 (1–3) (2013) 24–28, doi:10.1016/j.jnucmat.2013.01.349.

[18] M. Li, J.-H. You, J. Nucl. Mater. 465 (2015) 702–709, doi:10.1016/j.jnucmat.2015.07.007.

[19] V.Kh. Alimov, et al., J. Nucl. Mater. 375 (2) (2008) 192–201, doi:10.1016/j.jnucmat.2008.01.008.

[20] S. Lindig, et al., Phys. Scr. T145 (2011) 014039, doi:10.1088/0031-8949/2011/T145/014039.

[21] L. Gao, et al., Nucl. Fusion 54 (2014) 122003, doi:10.1088/0029-5515/54/12/122003.